

Hyperfine state-changing collisions of Cs($6P_{1/2}$) atoms with argon perturbers

L. Morgus,^{1,*}† T. Morgus,^{2,†} T. Drake,¹ and J. Huennekens³

¹*Department of Physics, 36 Madison Avenue, Drew University, Madison, New Jersey 07940, USA*

²*Department of Physics, 200 Prospect Street, East Stroudsburg University, East Stroudsburg, Pennsylvania 18301, USA*

³*Department of Physics, 16 Memorial Drive East, Lehigh University, Bethlehem, Pennsylvania 18015, USA*

(Received 6 November 2007; published 10 March 2008)

A two-step excitation experiment has been employed to measure the collisional rate coefficients and to study the velocity distribution of Cs($6P_{1/2}$) atoms that have undergone a single hyperfine state-changing collision with Ar. In addition, argon pressure broadening rates and shifts of the cesium $6P_{1/2}(F') \rightarrow 8S_{1/2}(F'')$ transitions have been determined. In the experiment, a single mode, cw Ti:sapphire laser is tuned to line center of the $6S_{1/2}(F=4) \rightarrow 6P_{1/2}(F'=3 \text{ or } 4)$ transition. Then, the frequency of a single mode cw dye laser is scanned over the $6P_{1/2} \rightarrow 8S_{1/2}$ manifold to probe the populations of the $6P_{1/2}$ hyperfine levels. Absorption of probe laser photons is monitored by detecting $8S_{1/2} \rightarrow 6P_{3/2}$ fluorescence. The experiment is conducted at room temperature, where the Cs density is low ($n \sim 3.4 \times 10^{10}$ atoms cm^{-3}), and thus the probability of a Cs-Cs collision is negligible during the Cs($6P_{1/2}$) radiative lifetime. The Ar pressure is varied from 0 to 1.52 Torr, and Cs-Ar collisions cause population to be transferred from the directly excited $6P_{1/2}(F')$ level to the other $6P_{1/2}$ hyperfine level. The data are analyzed using a density matrix formalism to yield the rate coefficients for Cs($6P_{1/2}$)-Ar hyperfine state-changing collisions. In addition, the one-dimensional velocity changing collision kernel for Cs($6P_{1/2}$) atoms prepared with $v_z=0$ that undergo $F'=3 \leftrightarrow F'=4$ hyperfine state-changing collisions with argon is reported.

DOI: [10.1103/PhysRevA.77.032704](https://doi.org/10.1103/PhysRevA.77.032704)

PACS number(s): 34.20.Cf, 32.10.Fn

I. INTRODUCTION

Velocity changing (VC) collision studies have proven to be a rich field [1–22] and are essential to the understanding of such phenomena as collision-broadened line shapes [4,9,10], diffusion of atoms in a vapor [15], and light-induced drift [5,6,8,18,23]. For ground state atoms, VC collisions are studied via atomic diffusion [15] and velocity-selective optical pumping (VSOP) [7,13,20] techniques. In contrast, the short lifetimes associated with excited states often preclude these types of studies. Instead, VC collision studies involving excited states are primarily investigated through the use of two-step–two-photon excitation [4,7,10], light-induced drift [5,6,8], and stimulated photon echo [22] experiments. Using the last of these techniques, Keller and Le Gouët have been able to extract van der Waals coefficients from measured VC collision cross sections [22].

Most previous research on VC collisions involving alkali-metal active atoms and noble gas perturbers has concentrated on elastic collisions and fine structure state-changing collisions [3,4,7,9,10,19,24–26] with far less focus on hyperfine state-changing collisions [27,28]. In particular, earlier two-step–two-photon excitation experiments [4,7,10] to study VC collisions have focused on excitation spectra for the $3S_{1/2} \rightarrow 3P_{1/2} \rightarrow 4D_{3/2}$ transitions of sodium atoms undergoing collisions with noble gas perturbers. Early measurements were used to determine thermalization rates and allowed for a comparison between observed line shapes and those calculated using simple collision models [4,7].

In the present work, a two-step–two-photon excitation experiment is employed to study cesium hyperfine state-changing collisions with argon buffer gas atoms. Our experimental setup and excitation scheme are discussed in Sec. II. The resulting data are presented in Sec. III along with the $6P_{1/2}(F') \rightarrow 8S_{1/2}(F'')$ argon pressure broadening rates and shifts. Section IV discusses the one-dimensional VC collision kernel for Cs($6P_{1/2}$) atoms prepared with $v_z=0$ that undergo $F'=3 \leftrightarrow F'=4$ hyperfine state-changing collisions, while Sec. V provides a detailed discussion of the density matrix formulation used to obtain the rate coefficients for Cs($6P_{1/2}$)-Ar hyperfine state-changing collisions. Finally, concluding remarks can be found in Sec. VI.

II. EXPERIMENT

The experimental setup is shown in Fig. 1, and a simplified energy-level diagram for cesium is shown in Fig. 2. Room temperature cesium atoms are contained in a cylindrical glass cell with a diameter of 3.56 cm and length of 13.97 cm that is initially evacuated to $P \sim 2 \times 10^{-6}$ Torr. At this temperature, the Cs density is low [29] ($n \sim 3.4 \times 10^{10}$ atoms cm^{-3}), and therefore, the probability of Cs-Cs collisions or radiation trapping is negligible. Argon can be added to the cell using the gas handling system shown in Fig. 1, and the argon pressure in the cell was varied from 0–1.52 Torr during the experiment. The presence of Ar perturbers can lead to Cs-Ar collisions that transfer population from the directly excited $6P_{1/2}(F')$ level to the other $6P_{1/2}$ hyperfine level.

A Coherent model 899-29 single mode, continuous wave (cw) titanium sapphire laser (the pump laser), pumped by a 10 W argon ion laser, was tuned to the cesium $6S_{1/2}(F=4)$

*lmorgus@thorlabs.com

†Present address: Thorlabs, Inc., 435 Route 206 North, Newton, NJ 07860.

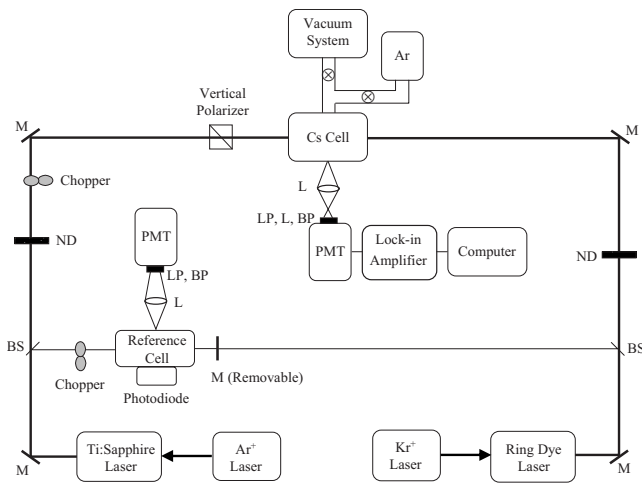


FIG. 1. Experimental setup. ND, LP, BP, and BS represent neutral density filter, longpass filter, bandpass filter, and beam splitter, respectively, while L, M, and PMT denote lens, mirror, and photomultiplier tube, respectively.

→ $6P_{1/2}(F'=3 \text{ or } 4)$ transition. The vertically polarized pump laser beam was directed through a series of neutral density filters such that the power at the cell was ~ 6 mW. Line center of the desired $6S_{1/2}(F=4) \rightarrow 6P_{1/2}(F')$ transition was found using saturation spectroscopy; a small portion of the pump laser beam was sent through a cesium reference cell and reflected back onto itself using a removable mirror mounted at the far end of the cell. The $6P_{1/2}(F') \rightarrow 6S_{1/2}(F)$ fluorescence signals, which exhibit Lamb dips,

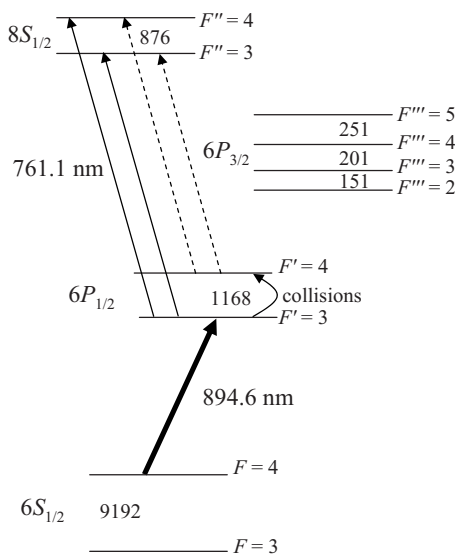


FIG. 2. Schematic energy-level diagram for cesium, which also indicates one possible pump-probe sequence. The pump transition is indicated by a thick solid arrow. Thin solid arrows denote those probe transitions that are possible from the directly populated $6P_{1/2}(F'=3)$ level, whereas dashed arrows indicate additional probe transitions that occur if Cs-Ar collisions transfer population to the $6P_{1/2}(F'=4)$ level. Transition wavelengths and hyperfine splittings, which have been greatly exaggerated for clarity and are not drawn to scale, are given in MHz.

were detected by a photodiode equipped with RG 715 and RG 850 longpass filters.

A Coherent model 699-29 single mode cw dye laser (the probe laser), pumped by a 4 W krypton ion laser, was then used to further excite the cesium atoms in the main cell from the $6P_{1/2}(F')$ level populated by the pump laser to $8S_{1/2}(F'')$ levels where $F''=3$ or 4. Using neutral density filters, the power of the vertically polarized probe beam was attenuated to $\sim 420 \mu\text{W}$ prior to entering the cell. The pump and probe laser beams counterpropagated through the cell, and their Gaussian beam diameters at the cell were determined to be 2.04 ± 0.10 mm and 2.30 ± 0.10 mm [full widths at half maximum], respectively. The criteria used to set the pump power were that the pump beam should be sufficiently intense to saturate the $6S_{1/2}(F=4) \rightarrow 6P_{1/2}(F')$ transition, thereby populating all the $m_{F'}$ levels approximately equally, while still being sufficiently weak so that power broadening remained negligible. The probe beam power was chosen to be as weak as possible while still maintaining a reasonable signal to noise ratio for the $6S_{1/2}(F$

$$\begin{aligned}
 &=4) \rightarrow 6P_{1/2}(F'=3) \xrightarrow{\text{collision}} 6P_{1/2}(F'=4) \rightarrow 8S_{1/2}(F''=3) \quad \text{or} \\
 &6S_{1/2}(F=4) \rightarrow 6P_{1/2}(F'=4) \xrightarrow{\text{collision}} 6P_{1/2}(F'=3) \rightarrow 8S_{1/2}(F''=4) \quad \text{collision-induced line shapes when 1 Torr of argon was added to the cell.}
 \end{aligned}$$

Absorption of probe laser photons was monitored by detecting $8S_{1/2} \rightarrow 6P_{3/2}$ fluorescence perpendicular to the laser propagation direction. Fluorescence from a 3.7 cm strip oriented along the laser propagation direction in the central region of the cell was imaged onto a free-standing Hamamatsu R636 photomultiplier tube equipped with two bandpass filters (both with $\lambda_0=790 \pm 5$ nm) and one RG 780 longpass filter. The pump beam was chopped and lock-in detection was employed. Since the narrow linewidth pump laser only excited atoms belonging to one velocity class ($v_z=0$ for this experiment) from the ground state $6S_{1/2}(F=4)$ level to the $6P_{1/2}(F')$ level of interest, the velocity distribution observed with the probe laser directly reflects the effects of VC collisions.

Removal of the indexer-mounted mirror from the reference cell path also enables the two-step $6S_{1/2}(F=4) \rightarrow 6P_{1/2}(F') \rightarrow 8S_{1/2}(F'')$ excitation of cesium atoms in the reference cell. Since the reference cell contains no argon perturbers, simultaneous detection of the $8S_{1/2} \rightarrow 6P_{3/2}$ fluorescence signals from both the main and reference cells allows for the determination of $6P_{1/2}(F') \rightarrow 8S_{1/2}(F'')$ argon pressure shifts.

III. EXPERIMENTAL RESULTS

Figure 3 shows typical excitation spectra observed as the probe laser was scanned over the $6P_{1/2} \rightarrow 8S_{1/2}$ manifold while exciting the cesium $6S_{1/2}(F=4) \rightarrow 6P_{1/2}(F'=3)$ transition with the pump laser (i.e., the excitation spectra associated with the pump-probe scheme illustrated in Fig. 2). As shown in Fig. 3(a), when no argon perturbers are present in the main cell, the two-step excitation process described above gives rise to a spectrum consisting of two transitions:

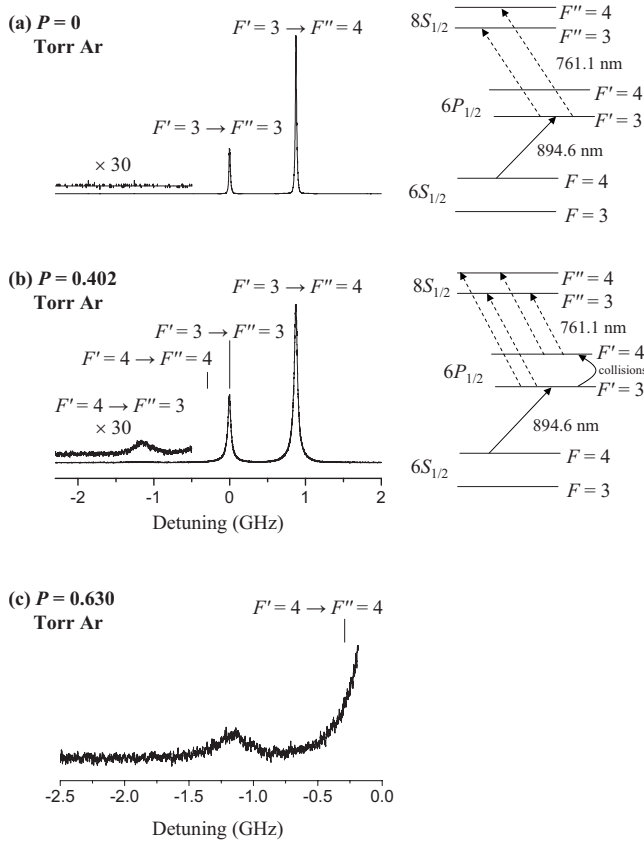


FIG. 3. Probe laser $6P_{1/2} \rightarrow 8S_{1/2}$ excitation spectra obtained with the pump laser fixed to line center of the $6S_{1/2}(F=4) \rightarrow 6P_{1/2}(F'=3)$ transition. (a) For $P=0$ Torr, two probe transitions are possible: $F'=3 \rightarrow F''=3$ and $F'=3 \rightarrow F''=4$. (b) For $P=0.402$ Torr, Cs-Ar collisions populate the $6P_{1/2}(F'=4)$ level and, hence, four probe transitions are possible: $F'=3 \rightarrow F''=3$, $F'=3 \rightarrow F''=4$, $F'=4 \rightarrow F''=3$, and $F'=4 \rightarrow F''=4$. Vertical lines indicate the line center positions of the $F'=3 \rightarrow F''=3$ and $F'=4 \rightarrow F''=4$ transitions. (c) Scan recorded at $P=0.630$ Torr showing the difficulty of resolving the weak $F'=4 \rightarrow F''=4$ collisional peak, which is buried in the red wing of the strong $F'=3 \rightarrow F''=3$ line. The zero of detuning marks the line center position of the $F'=3 \rightarrow F''=3$ transition.

$6S_{1/2}(F=4) \rightarrow 6P_{1/2}(F'=3) \rightarrow 8S_{1/2}(F''=3)$ and $6S_{1/2}(F=4) \rightarrow 6P_{1/2}(F'=3) \rightarrow 8S_{1/2}(F''=4)$. The observed lines are quite narrow due to the excitation of only one velocity class and because it is highly improbable for a VC collision to occur between a Cs atom and another Cs atom or any impurity atom present in the cell within one radiative lifetime. When argon buffer gas is introduced into the cell, the situation is quite different as shown in Fig. 3(b) for $P=0.402$ Torr. Now the $F'=3 \rightarrow F''=3$ and $F'=3 \rightarrow F''=4$ transitions exhibit some pressure broadening and the effects of VC collisions. In addition, a weak third peak corresponding to the $F'=4 \rightarrow F''=3$ transition is visible to the left of the two direct peaks. This third peak is quite broad since an inelastic collision with an Ar perturber, which can alter the Cs atom's velocity, is necessary to populate the $6P_{1/2}(F'=4)$ level. Hence the $6P_{1/2}(F'=4) \rightarrow 8S_{1/2}(F''=3)$ transition line shape provides a direct measure of the distribution of the compo-

nent of velocity along the laser propagation direction following a hyperfine state-changing collision. There is another weak collisional peak, which is associated with the $F'=4 \rightarrow F''=4$ transition, but it is buried in the red wing of the intense $F'=3 \rightarrow F''=3$ direct peak and cannot be resolved [see Fig. 3(c)].

In addition to pumping the $6S_{1/2}(F=4) \rightarrow 6P_{1/2}(F'=3)$ transition as shown in Fig. 2, data were also obtained by exciting the $6S_{1/2}(F=4) \rightarrow 6P_{1/2}(F'=4)$ pump transition. In this latter case, $F'=4 \rightarrow F''=3$ and $F'=4 \rightarrow F''=4$ are the two direct probe transitions whereas $F'=3 \rightarrow F''=3$ and $F'=3 \rightarrow F''=4$ are the two probe transitions that result when Cs atoms in the directly pumped $6P_{1/2}(F'=4)$ level are collisionally transferred to the $6P_{1/2}(F'=3)$ level.

The probe laser excitation peaks associated with levels directly populated by the pump laser [i.e., $6S_{1/2}(F=4) \rightarrow 6P_{1/2}(F'=3) \rightarrow 8S_{1/2}(F'')$ or $6S_{1/2}(F=4) \rightarrow 6P_{1/2}(F'=4) \rightarrow 8S_{1/2}(F'')$ with $F''=3$ or 4] were fit to Lorentzian profiles (since these line shapes are dominated by pressure broadening) in which the areas, line center peak locations, and FWHM were free parameters. The Lorentzian tail of the $F=4 \rightarrow F'=3 \rightarrow F''=3$ [$F=4 \rightarrow F'=4 \rightarrow F''=4$] transition was then subtracted from the baseline of the

$6S_{1/2}(F=4) \rightarrow 6P_{1/2}(F'=3) \xrightarrow{\text{collision}} 6P_{1/2}(F'=4) \rightarrow 8S_{1/2}(F''=3)$ [$6S_{1/2}(F=4) \rightarrow 6P_{1/2}(F'=4) \xrightarrow{\text{collision}} 6P_{1/2}(F'=3) \rightarrow 8S_{1/2}(F''=4)$] line shape, and the remaining peak was integrated to obtain the collisional peak area. Figure 4 shows a comparison of the resulting Lorentzian fit to the experimental data when the cell contains 0.153 Torr of Ar and the pump laser is tuned to the $6S_{1/2}(F=4) \rightarrow 6P_{1/2}(F'=3)$ transition. In addition, the last frame of the figure shows the collisional peak [$6S_{1/2}(F=4) \rightarrow 6P_{1/2}(F'=3) \xrightarrow{\text{collision}} 6P_{1/2}(F'=4) \rightarrow 8S_{1/2}(F''=3)$] that remains following subtraction of the Lorentzian tail corresponding to the nearby $F=4 \rightarrow F'=3 \rightarrow F''=3$ line shape.

From the FWHM of the direct peak experimental line shapes, it is straightforward to determine the $6P_{1/2}(F') \rightarrow 8S_{1/2}(F'')$ argon pressure broadening rates. Furthermore, a comparison of the direct peak line center frequencies for excitation spectra acquired from the main cell to those simultaneously recorded using the reference cell, which contains no argon gas, allows the argon pressure shift to be determined. Figure 5(a) shows how the addition of argon to the main cell affects the width and center frequency of the $F=4 \rightarrow F'=3 \rightarrow F''=4$ transition line shape, while Fig. 5(b) shows a plot of the $6P_{1/2}(F') \rightarrow 8S_{1/2}(F'')$ linewidth Γ and line center shift Γ_{shift} as a function of the argon density n_{Ar} in the cell for each direct $6P_{1/2}(F') \rightarrow 8S_{1/2}(F'')$ probe transition where F' and $F''=3$ or 4. The linewidth Γ is given by

$$\Gamma = \Gamma' + \Gamma_{\text{Br}}, \quad (1)$$

where Γ' is the natural linewidth (we note that Γ' should also include the effects of power broadening and instrumental resolution, but these were found to be negligible in the present case) and Γ_{Br} is the Cs[$6P_{1/2}(F') \rightarrow 8S_{1/2}(F'')$] argon

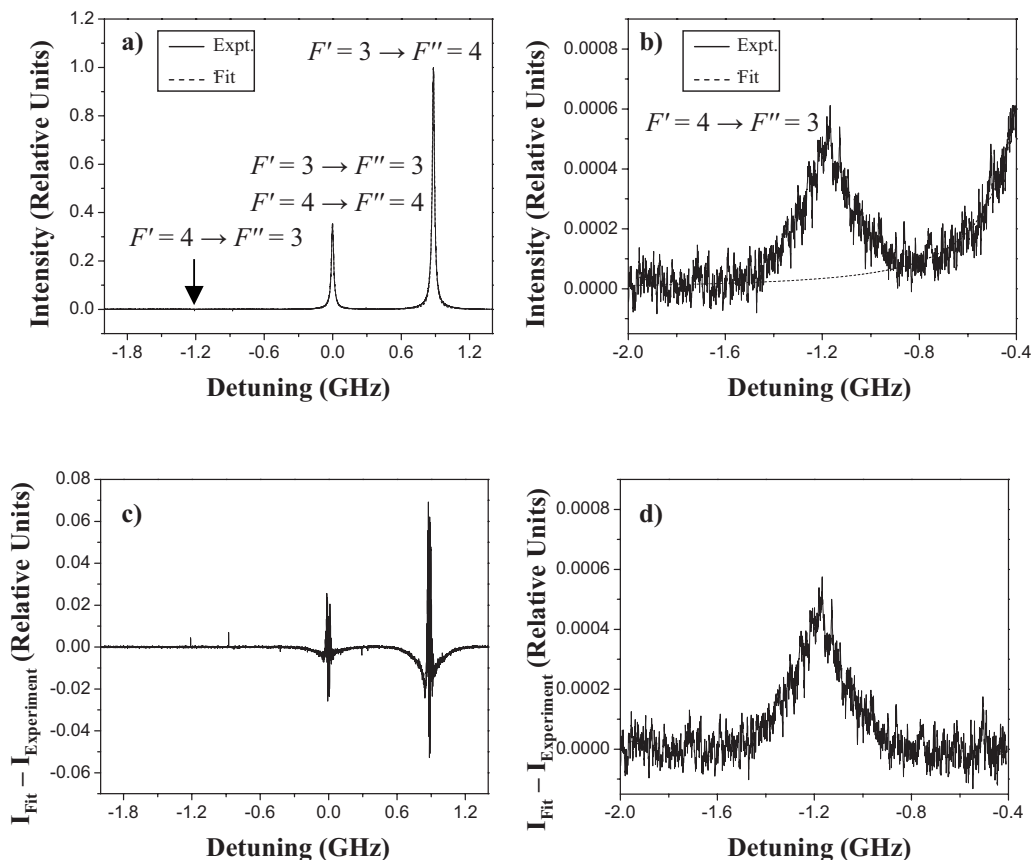


FIG. 4. Comparison of the experimental data to the fit when $P=0.153$ Torr and the pump laser is tuned to the Cs $6S_{1/2}(F=4) \rightarrow 6P_{1/2}(F'=3)$ transition. Relative units for intensities are the same for all four panels. (a) The $F'=3 \rightarrow F''=3$ and $F'=3 \rightarrow F''=4$ transitions were each fit with a three parameter Lorentzian profile (dashed lines) and then compared to the experimental excitation spectra (solid lines). (b) The $F'=4 \rightarrow F''=3$ collisional line shape (solid line) plotted with the Lorentzian tail of the $F'=3 \rightarrow F''=3$ transition line shape (dashed line). (c) Residual showing the quality of the fit in frame (a). (d) Subtraction of the $F'=3 \rightarrow F''=3$ Lorentzian tail from the collisional line shape in frame (b) gives the corrected collisional line shape shown here, which is numerically integrated to yield the collisional peak area.

pressure broadening rate, which is related to the argon pressure broadening rate coefficient k_{Br} via

$$\Gamma_{Br} = k_{Br} n_{Ar}. \quad (2)$$

Figure 5(b) also shows the line center shift Γ_{shift} for each Cs[$6P_{1/2}(F') \rightarrow 8S_{1/2}(F'')$] transition, which is related to the argon pressure shift coefficient k_{shift} via

$$\Gamma_{shift} = k_{shift} n_{Ar}. \quad (3)$$

Although the uncertainties in the widths of the fitted Lorentzians were taken into consideration, the uncertainty in each individual Γ value was dominated by the uncertainty in the argon pressure (and hence n_{Ar}). The manufacturer's stated accuracy of the Baratron M626A Capacitance Manometer used in this experiment is 0.15% of the reading; however, we believe that a more realistic uncertainty in the pressure reading (given that the capacitance manometer is located close to, but not directly inside, the main cell) is ± 0.03 Torr. Based on this, the contribution to the total error assigned to each individual Γ value due to the uncertainty in the argon pressure ranged from $\sim 2\%$ (for the highest pressure data) to $\sim 56\%$ (for the lowest pressure data). The un-

certainty of the fitted Lorentzian width contributed an additional 0.1–2 % to the overall error. In the case of Γ_{shift} , error bars reflect the uncertainty of the line center frequency of the Lorentzian profile fit and the uncertainty in the argon pressure. Once again, the uncertainty in the pressure is the dominant contribution to the overall error bars.

The Cs[$6P_{1/2}(F') \rightarrow 8S_{1/2}(F'')$] argon pressure broadening rate coefficients and shift coefficient as determined from Fig. 5(b) are listed in Table I. Since the differences between the k_{Br} values for the various Cs[$6P_{1/2}(F') \rightarrow 8S_{1/2}(F'')$] transitions are greater than the uncertainties in the values, our

TABLE I. Cs[$6P_{1/2}(F') \rightarrow 8S_{1/2}(F'')$] argon pressure broadening rate coefficients and pressure shift coefficient determined from Fig. 5(b).

Transition	k_{Br} ($\text{cm}^3 \text{sec}^{-1}$)	k_{shift} ($\text{cm}^3 \text{sec}^{-1}$)
$F'=3 \rightarrow F''=3$	$(2.24 \pm 0.05) \times 10^{-8}$	
$F'=3 \rightarrow F''=4$	$(2.38 \pm 0.04) \times 10^{-8}$	
$F'=4 \rightarrow F''=3$	$(2.69 \pm 0.04) \times 10^{-8}$	$(-4.83 \pm 0.04) \times 10^{-9}$
$F'=4 \rightarrow F''=4$	$(2.48 \pm 0.04) \times 10^{-8}$	

results suggest that we have been able to isolate the effects of pressure broadening due to Ar for each individual hyperfine component. Conversely, the shift rates of the four transitions were found to be equal within error bars, and thus only the average value is reported. The reported $6P_{1/2}(F') \rightarrow 8S_{1/2}(F'')$ argon pressure broadening rate coefficients should serve as a sensitive test of the quality of theoretical models for long range Cs[$6P_{1/2}(F')$]-Ar and Cs[$8S_{1/2}(F'')$]-Ar interatomic potentials.

IV. ONE-DIMENSIONAL VELOCITY CHANGING COLLISION KERNEL

By keeping the Ar pressure sufficiently low such that only a small fraction of the atoms in the $6P_{1/2}(F')$ level populated by the pump laser is transferred to the other hyperfine level, it can be assumed that the data are taken in the single collision regime [i.e., it is unlikely for a Cs atom to experience more than one Cs-Ar collision during the Cs $6P_{1/2}(F')$ radiative lifetime]. As a result, it follows that when the probe laser frequency is scanned across the transition from the collisionally populated $6P_{1/2}(F')$ level to the $8S_{1/2}(F'' \neq F')$ level, we observe the velocity distribution of the Cs $6P_{1/2}(F')$ atoms that have each undergone a single hyperfine state-changing collision. Therefore, our data enables us to measure the one-dimensional VC collision kernel of $6P_{1/2}$ atoms that are prepared with $v_z=0$ and undergo an $F'=3 \leftrightarrow F'=4$ hyperfine state-changing collision. The one-dimensional VC collision kernel $W(v_z \rightarrow v'_z)$ is the probability that a cesium atom's initial velocity v_z is changed to v'_z as a result of a collision with an argon atom belonging to a thermal distribution. The collisional line shape is a direct measure of $W(v_z \rightarrow v'_z)$. Nominally, either $6P_{1/2}(F') \rightarrow 8S_{1/2}(F''=3 \text{ or } 4)$ transition from the collisionally populated $6P_{1/2}(F')$ level should exhibit the effects of VC collisions; however, as mentioned in Sec. III, the excitation spectrum associated with $F'=F''$ is

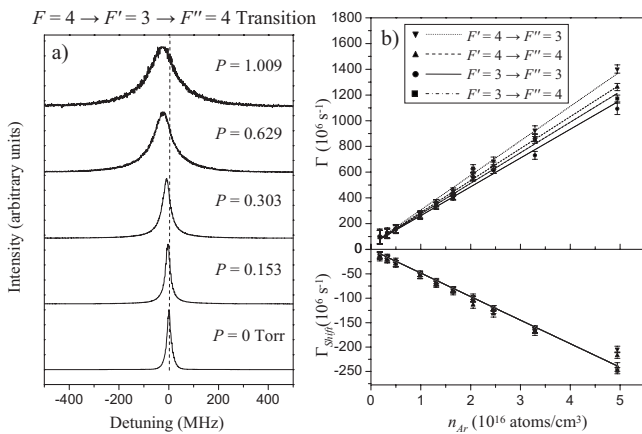


FIG. 5. (a) $6P_{1/2}(F'=3) \rightarrow 8S_{1/2}(F''=4)$ excitation spectra demonstrating the effects of argon buffer gas on the transition linewidth and line center frequency. (b) The $6P_{1/2}(F') \rightarrow 8S_{1/2}(F'')$ linewidth Γ (FWHM in angular frequency units) and line center shift Γ_{shift} as functions of argon density n_{Ar} for each direct $6P_{1/2}(F') \rightarrow 8S_{1/2}(F'')$ probe transition.

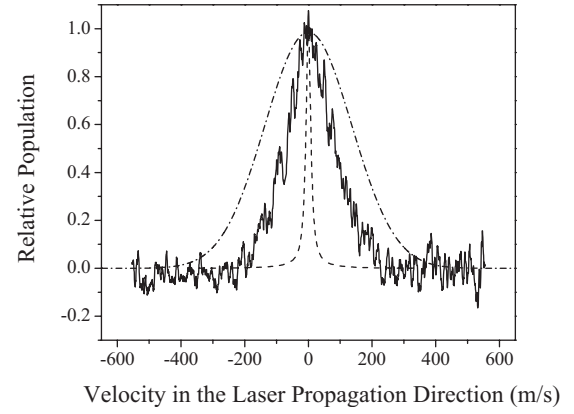


FIG. 6. One-dimensional VC collision kernel for Cs[$6P_{1/2}(F'=3)$]+Ar \rightarrow Cs[$6P_{1/2}(F'=4)$]+Ar collisions (as traced out by the Doppler-broadened probe transition line shapes). The normalized velocity distribution (along the laser propagation direction) is shown for the directly excited $6S_{1/2}(F=4) \rightarrow 6P_{1/2}(F'=3) \rightarrow 8S_{1/2}(F''=4)$ transition (dashed line), the collisionally populated $6S_{1/2}(F=4) \rightarrow 6P_{1/2}(F'=3) \xrightarrow{\text{collision}} 6P_{1/2}(F'=4) \rightarrow 8S_{1/2}(F''=3)$ transition (solid line), and a thermal distribution (dashed-dotted line). It can be seen that significant redistribution of velocity occurs in a single hyperfine state-changing collision, but complete thermalization does not result. For these measurements, the pump and probe laser powers were ~ 3.6 mW and ~ 2.5 mW, respectively.

not resolvable from one of the transitions involving the directly populated $6P_{1/2}$ hyperfine level.

Figure 6 shows the measured, normalized $6S_{1/2}(F=4) \rightarrow 6P_{1/2}(F'=3) \rightarrow 8S_{1/2}(F''=4)$ excitation line shape [dominated by the homogeneous line shape associated with the initially prepared $v_z=0$ component in the $6P_{1/2}(F'=3)$ level],

the measured $6S_{1/2}(F=4) \rightarrow 6P_{1/2}(F'=3) \xrightarrow{\text{collision}} 6P_{1/2}(F'=4) \rightarrow 8S_{1/2}(F''=3)$ line shape [reflecting the velocity distribution in the $6P_{1/2}(F'=4)$ level following one hyperfine state-changing collision], and a theoretical Doppler line shape corresponding to a $6P_{1/2}$ thermal velocity distribution at the cell temperature. For this VC collision line shape measurement, the pump and probe laser powers were increased to ~ 3.6 mW and ~ 2.5 mW, respectively, leading to a better signal to noise ratio. From the figure it is evident that, in general, an $F'=3 \leftrightarrow F'=4$ hyperfine state-changing collision does in fact change the component of a Cs atom's velocity along the laser propagation direction. However, it is also clear that a single collision is not sufficient to thermalize the $6P_{1/2}(F'=4)$ velocity distribution completely. Although Fig.

6 shows the results of $6P_{1/2}(F'=3) \xrightarrow{\text{collision}} 6P_{1/2}(F'=4)$ collisional transfer, the measured Cs atom velocity distribution along the laser propagation direction following

$6P_{1/2}(F'=4) \xrightarrow{\text{collision}} 6P_{1/2}(F'=3)$ collisional transfer is identical, within experimental uncertainties. Velocity distributions recorded with lower pump and probe laser powers (such as those used to measure the hyperfine state-changing collision rate coefficients) are consistent but noisier.

Previous two-step excitation studies of sodium in the presence of low pressure noble gas perturbers were carried out by O'Callaghan and Gallagher to study $\text{Na}(3P_{3/2}) \rightarrow \text{Na}(3P_{1/2})$ fine structure state-changing collisions in the single collision limit [10]. Their results show a relatively narrow velocity distribution in the $3P_{1/2}$ state following excitation of $3P_{3/2}$, even though these two levels are separated by 17.2 cm^{-1} , which implies that velocity changes in fine structure state-changing collisions are generally small. In contrast, the data presented here demonstrate that the velocity changes occurring in Cs $6P_{1/2}$ hyperfine state-changing collisions are much larger than those measured by O'Callaghan and Gallagher. This seems to indicate that a hyperfine state-changing collision process requires a strong collision at small impact parameter, thereby leading to large velocity changes.

V. HYPERFINE STATE-CHANGING COLLISION RATE COEFFICIENT

This section discusses the analysis of our data using a density matrix formalism to determine Cs $6P_{1/2}(F')$ -Ar hyperfine state-changing collision rate coefficients. The density matrix approach allows coherence effects (which are neglected in a simpler rate equation model) to be taken into account. Although all 80 magnetic sublevels of the cesium $6S_{1/2}$, $6P_{1/2}$, $8S_{1/2}$, and $6P_{3/2}$ states were incorporated into our density matrix analysis, for discussion purposes Fig. 7 shows a simplified six level system and one possible pump-probe scheme. The various collisional and radiative rates to be considered are also shown in the figure.

Levels 1 and 2 represent the two hyperfine levels of the Cs ground state. In our experiment, we always excite atoms out of the $6S_{1/2}(F=4)$ hyperfine level (i.e., level 1) and thus the $6S_{1/2}(F=3)$ hyperfine level (level 2) serves as a trap level that is coupled radiatively to the excited levels 3, 4, and 6 but not to level 1. In the absence of collisions, atoms in any of the ground or excited state energy levels pass through the laser beams as a result of thermal motion and are effectively replaced by atoms belonging to any of the magnetic sublevels of the $6S_{1/2}(F=3)$ and $6S_{1/2}(F=4)$ ground state hyperfine levels. An effective transit relaxation rate coefficient Γ_t was derived by Sagle *et al.* and is given by [30]

$$\Gamma_t = 1.13 \frac{v_{\text{rms}}}{D} \approx 1.07 \times 10^5 \text{ s}^{-1}, \quad (4)$$

where v_{rms} is the two-dimensional root-mean-square atomic velocity for Cs at the cell temperature ($T \sim 23 \text{ }^\circ\text{C}$ in the present case) and D is the Gaussian beam diameter (FWHM) of the pump laser. We assume that each level is depleted by transit relaxation at a rate Γ_t , and each magnetic sublevel of the ground state is populated statistically; therefore the transit relaxation rate from level 1 to level 2 is $(7/16)\Gamma_t$, while the corresponding rate from level 2 to level 1 is $(9/16)\Gamma_t$.

In the experiment, the $6S_{1/2}(F=4)$ hyperfine level is coupled to either the $6P_{1/2}(F'=3)$ or the $6P_{1/2}(F'=4)$ state via a monochromatic, linearly polarized pump laser. Hyperfine state-changing collisions (represented by R_{34} and R_{43} in

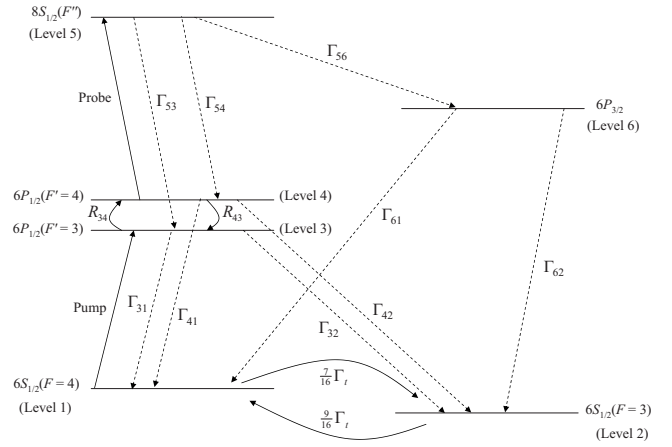


FIG. 7. Simplified six-level energy level diagram used to illustrate the basic features of the complete 80 level system analyzed via a density matrix formalism. For this simplified scheme, the magnetic sublevels that comprise the $6S_{1/2}(F=3)$, $6S_{1/2}(F=4)$, $6P_{1/2}(F'=3)$, $6P_{1/2}(F'=4)$, $8S_{1/2}$, and $6P_{3/2}$ states of cesium are indistinguishable, whereas in the 80 level scheme the $2F+1$ magnetic sublevels that comprise a particular hyperfine level are considered to be distinct but degenerate in energy. One possible pump-probe scheme is shown (i.e., pump: $F=4 \rightarrow F'=3$; probe: $F'=4 \rightarrow F''$ where $F''=3$ or 4). Γ_{ij} represents a radiative rate and R_{ij} a collisional rate for transfer of population from level i to level j . Transit relaxation between the ground state hyperfine levels [at rates $(7/16)\Gamma_t$ and $(9/16)\Gamma_t$] is also indicated. Transit relaxation from each of the excited states to the $6S_{1/2}(F=3)$ and $6S_{1/2}(F=4)$ levels [at rates $(7/16)\Gamma_t$ and $(9/16)\Gamma_t$, respectively] is also considered in the model but not shown in the figure.

Fig. 7) transfer population between the $6P_{1/2}(F'=3)$ and $6P_{1/2}(F'=4)$ states (again distributing population statistically over the final state magnetic sublevels). For the pressures used in this experiment, Cs-Ar collisions transfer less than 1% of the population of the directly excited $6P_{1/2}(F')$ level (i.e., level 3 in the figure) to the other $6P_{1/2}$ hyperfine component (level 4). Back transfer from the collisionally populated level back to the directly populated level is also taken into consideration in the model even though contributions to level populations from this type of collision are extremely small (i.e., $\sim 0.01\%$).

The linearly polarized probe laser is used to couple the $6P_{1/2}(F'=3)$ or $6P_{1/2}(F'=4)$ state to one of the hyperfine levels of the $8S_{1/2}$ state. Thus, level 5 in Fig. 7 can be assigned to either the $8S_{1/2}(F''=3)$ or the $8S_{1/2}(F''=4)$ state depending on the probe transition selected. If the pump-probe scheme is $6S_{1/2}(F=4) \rightarrow 6P_{1/2}(F') \rightarrow 8S_{1/2}(F'')$, the resulting $8S_{1/2}(F'')$ level population provides information about the population in the directly pumped $6P_{1/2}(F')$ level. Alternatively, when the pump-probe scheme is $6S_{1/2}(F=4) \rightarrow 6P_{1/2}(F'=3)/6P_{1/2}(F'=4) \rightarrow 8S_{1/2}(F'')$ (as illustrated in Fig. 7) or $6S_{1/2}(F=4) \rightarrow 6P_{1/2}(F'=4)/6P_{1/2}(F'=3) \rightarrow 8S_{1/2}(F'')$, then information about the collisionally populated $6P_{1/2}(F')$ level is obtained. Hence, for a given pump laser transition, four different probe schemes are considered: $6P_{1/2}(F'=3) \rightarrow 8S_{1/2}(F''=3)$, $6P_{1/2}(F'=3) \rightarrow 8S_{1/2}(F''=4)$, $6P_{1/2}(F'=4) \rightarrow 8S_{1/2}(F''=3)$, and $6P_{1/2}(F'=4) \rightarrow 8S_{1/2}(F''=4)$.

=4), two of which correspond to strong direct peaks and two corresponding to weak collisional peaks [see Fig. 3(b)].

In the analysis, we assume that the pump laser frequency is fixed to the center of the transition so that only one velocity component ($v_z=0$) is excited. In general, the density matrix equations of motion are given by [31]

$$\dot{\rho}_{ij} = -\frac{i}{\hbar} \sum_k (H_{ik}\rho_{kj} - \rho_{ik}H_{kj}) + \text{relaxation terms}, \quad (5)$$

where the relaxation terms include collisional and radiative transfer of population, transit relaxation, and collisional decoherence. The density matrix equations applicable to the pump-probe scheme depicted in Fig. 7 are the following [32]:

$$\begin{aligned} \dot{\rho}_{11} = & -\frac{7}{16}\Gamma_t\rho_{11} + \frac{9}{16}\Gamma_t\rho_{22} + \left(\Gamma_{31} + \frac{9}{16}\Gamma_t\right)\rho_{33} \\ & + \left(\Gamma_{41} + \frac{9}{16}\Gamma_t\right)\rho_{44} + \frac{9}{16}\Gamma_t\rho_{55} + \left(\Gamma_{61} + \frac{9}{16}\Gamma_t\right)\rho_{66} \\ & + \frac{i}{\hbar}(V_{31}\rho_{13} - \rho_{31}V_{13}) = 0, \end{aligned} \quad (6)$$

$$\begin{aligned} \dot{\rho}_{22} = & \frac{7}{16}\Gamma_t\rho_{11} - \frac{9}{16}\Gamma_t\rho_{22} + \left(\Gamma_{32} + \frac{7}{16}\Gamma_t\right)\rho_{33} \\ & + \left(\Gamma_{42} + \frac{7}{16}\Gamma_t\right)\rho_{44} + \frac{7}{16}\Gamma_t\rho_{55} + \left(\Gamma_{62} + \frac{7}{16}\Gamma_t\right)\rho_{66} \\ = & 0, \end{aligned} \quad (7)$$

$$\begin{aligned} \dot{\rho}_{33} = & -(\Gamma_3 + R_{34} + \Gamma_t)\rho_{33} + R_{43}\rho_{44} + \Gamma_{53}\rho_{55} \\ & - \frac{i}{\hbar}(V_{31}\rho_{13} - \rho_{31}V_{13}) = 0, \end{aligned} \quad (8)$$

$$\begin{aligned} \dot{\rho}_{44} = & R_{34}\rho_{33} - (\Gamma_4 + R_{43} + \Gamma_t)\rho_{44} + \Gamma_{54}\rho_{55} \\ & + \frac{i}{\hbar}(V_{54}\rho_{45} - \rho_{54}V_{45}) = 0, \end{aligned} \quad (9)$$

$$\dot{\rho}_{55} = -(\Gamma_5 + \Gamma_t)\rho_{55} - \frac{i}{\hbar}(V_{54}\rho_{45} - \rho_{54}V_{45}) = 0, \quad (10)$$

$$\dot{\rho}_{66} = \Gamma_{56}\rho_{55} - (\Gamma_6 + \Gamma_t)\rho_{66} = 0, \quad (11)$$

$$\dot{\rho}_{31} = -(i\omega_{31} + \delta_{31} + \Gamma_t)\rho_{31} + \frac{i}{\hbar}V_{31}(\rho_{33} - \rho_{11}), \quad (12)$$

and

$$\dot{\rho}_{54} = -(i\omega_{54} + \delta_{54} + \Gamma_t)\rho_{54} + \frac{i}{\hbar}V_{54}(\rho_{55} - \rho_{44}). \quad (13)$$

Here, the diagonal elements of the density matrix $\rho_{ii} \equiv n_i$ represent the level populations (normalized such that

$$\sum_i \rho_{ii} = 1$$

whereas the off-diagonal elements ρ_{ij} represent the coherences between levels i and j ; the latter will be nonzero only if the two levels are coupled by the coherent field of a laser. Γ_{ij} is the rate for radiative transitions from level i to level j and the total radiative rate out of a level i is denoted by

$$\Gamma_i \equiv \sum_j \Gamma_{ij}.$$

δ_{ij} is the coherence decay rate [i.e., the homogeneous linewidth (HWHM)], $\omega_{ij} = (E_i - E_j)/\hbar$ is the transition frequency (in angular frequency units), $E_i = H_{ii}$ is the energy of level i , and $V_{ij} = H_{ij}$ (for $i \neq j$) is the average interaction energy between an atom and a laser photon tuned near the $j \rightarrow i$ transition. We note that [32,33]

$$|V_{ij}|^2 = \frac{\hbar\Gamma_{ij}\lambda^3 I(r)}{16\pi^2 c}, \quad (14)$$

where $I(r)$ is the laser intensity at a radial distance r from the beam axis. For our calculations, we ignore the radial intensity variations and instead model the beam intensities as if they were uniform and given by the average laser intensities obtained from the measured laser powers and beam radii reported in Sec. II. Also, by definition, $\rho_{ij} = \rho_{ji}^*$ and $V_{ij} = V_{ji}^*$. In steady state, all of the populations are time independent, and therefore we require that $\dot{\rho}_{11} = \dot{\rho}_{22} = \dot{\rho}_{33} = \dot{\rho}_{44} = \dot{\rho}_{55} = \dot{\rho}_{66} = 0$.

By invoking the rotating wave approximation [32], the off-diagonal density matrix component ρ_{ij} can be written as

$$\rho_{ij} = \sigma_{ij}e^{-i\omega t}, \quad (15)$$

where ω is the laser frequency and σ_{ij} varies slowly (i.e., we can neglect $\dot{\sigma}_{ij}$). Substitution of this result into either Eq. (12) or (13) yields an equation of the form

$$\dot{\rho}_{ij} = -i\omega\rho_{ij} = -(i\omega_{ij} + \delta_{ij} + \Gamma_t)\rho_{ij} + \frac{i}{\hbar}V_{ij}(\rho_{ii} - \rho_{jj}) \quad (16)$$

or

$$[i\Delta_{ij} - (\delta_{ij} + \Gamma_t)]\rho_{ij} + \frac{iV_{ij}}{\hbar}(\rho_{ii} - \rho_{jj}) = 0, \quad (17)$$

where $\Delta_{ij} = \omega - \omega_{ij}$ is the detuning of the laser from line center, which is taken to be zero in our analysis. Finally, solving for the off diagonal density matrix element, we obtain

$$\begin{aligned} \rho_{ij} = & \frac{i}{\hbar}V_{ij} \frac{(\rho_{ii} - \rho_{jj})}{[-i\Delta_{ij} + (\delta_{ij} + \Gamma_t)]} \\ = & \frac{V_{ij}}{\hbar} \frac{[-\Delta_{ij} + i(\delta_{ij} + \Gamma_t)]}{[(\Delta_{ij})^2 + (\delta_{ij} + \Gamma_t)^2]} (\rho_{ii} - \rho_{jj}). \end{aligned} \quad (18)$$

Substitution of Eq. (18) into Eqs. (7)–(11) yields five coupled equations with six unknowns. Equation (6) is not independent of Eqs. (7)–(11), but the normalization constraint $\sum_i \rho_{ii} = 1$ provides one additional equation.

For the case where we probe the directly excited $6P_{1/2}(F')$ level (i.e., level 3 in Fig. 7), the density matrix

equations become more complicated since there is a third coherence term ρ_{51} (in addition to ρ_{31} and ρ_{53}). The density matrix equations for the diagonal elements in this case are the following:

$$\begin{aligned} \dot{\rho}_{11} = & -\frac{7}{16}\Gamma_t\rho_{11} + \frac{9}{16}\Gamma_t\rho_{22} + \left(\Gamma_{31} + \frac{9}{16}\Gamma_t\right)\rho_{33} \\ & + \left(\Gamma_{41} + \frac{9}{16}\Gamma_t\right)\rho_{44} + \frac{9}{16}\Gamma_t\rho_{55} + \left(\Gamma_{61} + \frac{9}{16}\Gamma_t\right)\rho_{66} \\ & + \frac{i}{\hbar}(V_{31}\rho_{13} - \rho_{31}V_{13}) = 0, \end{aligned} \quad (19)$$

$$\begin{aligned} \dot{\rho}_{22} = & \frac{7}{16}\Gamma_t\rho_{11} - \frac{9}{16}\Gamma_t\rho_{22} + \left(\Gamma_{32} + \frac{7}{16}\Gamma_t\right)\rho_{33} \\ & + \left(\Gamma_{42} + \frac{7}{16}\Gamma_t\right)\rho_{44} + \frac{7}{16}\Gamma_t\rho_{55} + \left(\Gamma_{62} + \frac{7}{16}\Gamma_t\right)\rho_{66} \\ = & 0, \end{aligned} \quad (20)$$

$$\begin{aligned} \dot{\rho}_{33} = & -(\Gamma_3 + R_{34} + \Gamma_t)\rho_{33} + R_{43}\rho_{44} + \Gamma_{53}\rho_{55} \\ & - \frac{i}{\hbar}(V_{31}\rho_{13} - \rho_{31}V_{13}) + \frac{i}{\hbar}(V_{53}\rho_{35} - \rho_{53}V_{35}) = 0, \end{aligned} \quad (21)$$

$$\dot{\rho}_{44} = R_{34}\rho_{33} - (\Gamma_4 + R_{43} + \Gamma_t)\rho_{44} + \Gamma_{54}\rho_{55} = 0, \quad (22)$$

$$\dot{\rho}_{55} = -(\Gamma_5 + \Gamma_t)\rho_{55} - \frac{i}{\hbar}(V_{53}\rho_{35} - \rho_{53}V_{35}) = 0, \quad (23)$$

and

$$\dot{\rho}_{66} = \Gamma_{56}\rho_{55} - (\Gamma_6 + \Gamma_t)\rho_{66} = 0. \quad (24)$$

Using the rotating wave approximation, the equations for the time derivatives of the off diagonal elements $\dot{\rho}_{31}$, $\dot{\rho}_{53}$, and $\dot{\rho}_{51}$ yield

$$[i\Delta_{31} - (\delta_{31} + \Gamma_t)]\rho_{31} + \frac{i}{\hbar}V_{31}(\rho_{33} - \rho_{11}) - \frac{i}{\hbar}V_{35}\rho_{51} = 0, \quad (25)$$

$$[i\Delta_{53} - (\delta_{53} + \Gamma_t)]\rho_{53} + \frac{i}{\hbar}V_{53}(\rho_{55} - \rho_{33}) + \frac{i}{\hbar}V_{13}\rho_{51} = 0, \quad (26)$$

and

$$[i(\Delta_{53} + \Delta_{31}) - (\delta_{51} + \Gamma_t)]\rho_{51} + \frac{i}{\hbar}V_{31}\rho_{53} - \frac{i}{\hbar}V_{53}\rho_{31} = 0, \quad (27)$$

respectively. Although the mathematics is slightly more complicated in this case, the coupled coherence equations (25)–(27) can still be solved to yield expressions for $(V_{31}\rho_{13} - \rho_{31}V_{13})$ and $(V_{53}\rho_{35} - \rho_{53}V_{35})$. With these expressions substituted into Eqs. (20)–(24), and using the constraint

$\sum_i \rho_{ii} = 1$, we again obtain six equations in six unknowns.

As mentioned above, in our full analysis, all 80 magnetic sublevels of the $6S_{1/2}(F=3)$, $6S_{1/2}(F=4)$, $6P_{1/2}(F'=3)$, $6P_{1/2}(F'=4)$, $8S_{1/2}$, and $6P_{3/2}$ states of cesium are considered in the density matrix formalism, thus leading to an 80×80 matrix. Within each hyperfine level, the $2F+1$ magnetic sublevels are considered to be distinct but degenerate in energy. This assumption is reasonable since a measurement of the magnetic field at the location of the cell indicates that it is ~ 0.53 G (i.e., dominated by the earth's magnetic field), and consequently, the Zeeman splittings are less than 1 MHz. Therefore, the pump laser couples the magnetic sublevels of the $6S_{1/2}(F=4)$ hyperfine level either to the seven magnetic sublevels of the $6P_{1/2}(F'=3)$ state or to the nine magnetic sublevels of the $6P_{1/2}(F'=4)$ state in accordance with the selection rule $\Delta m_F = 0$ for linearly polarized light and the restriction that the $6S_{1/2}(F=4, m_F=0) \rightarrow 6P_{1/2}(F'=4, m_{F'}=0)$ transition is forbidden. Similarly, the linearly polarized probe laser couples magnetic sublevels of the $6P_{1/2}$ and $8S_{1/2}$ states, again adhering to the $\Delta m_F = 0$ selection rule and the fact that in this case the $6P_{1/2}(F', m_{F'}=0) \rightarrow 8S_{1/2}(F''=F', m_{F''}=0)$ transitions are forbidden.

When considering the density matrix equations for the individual magnetic sublevels, we must also consider how hyperfine state-changing collisions, $6P_{1/2}(F'=3) + \text{Ar} \leftrightarrow 6P_{1/2}(F'=4) + \text{Ar}$, redistribute population among the $m_{F'}$ sublevels. We will see that collisional excitation transfer from one hyperfine level to another requires strong collisions at small impact parameters. Thus our model assumes that the hyperfine state-changing collisions effectively scramble $m_{F'}$ (i.e., that collisional transitions from a particular $m_{F'}$ sublevel of the initial state are equally likely to populate any $m_{F'}$ level of the final state). In this case, the principle of detailed balance [34] indicates that

$$\frac{k_{6P_{1/2}(F'=4 \rightarrow F'=3)}^{\text{hfs}}}{k_{6P_{1/2}(F'=3 \rightarrow F'=4)}^{\text{hfs}}} = \frac{g_3 e^{+\Delta E/k_B T}}{g_4} = \frac{7}{9} = 0.78, \quad (28)$$

where g_3 and g_4 are the statistical weights ($2F'+1$) of the $F'=3$ and $F'=4$ levels, respectively, and $k_{6P_{1/2}(F'=i \rightarrow F'=j)}^{\text{hfs}}$ is the collisional rate coefficient. We note that the energy gap $E_{F'=4} - E_{F'=3} \ll k_B T$ in the above expression, so the exponential factor is ≈ 1 . The appropriate hyperfine state-changing collision rates are given by $R_{34} = k_{6P_{1/2}(F'=3 \rightarrow F'=4)}^{\text{hfs}} n_{\text{Ar}}$ and $R_{43} = k_{6P_{1/2}(F'=4 \rightarrow F'=3)}^{\text{hfs}} n_{\text{Ar}}$.

Atoms in all levels leave the excitation region due to thermal motion and are effectively replaced by ground state atoms occupying any of the 16 ground state hyperfine magnetic sublevels. Consequently, the transit relaxation rate corresponding to effective transitions from a particular magnetic sublevel of any ground or excited level to each of the 16 magnetic sublevels of the $6S_{1/2}(F=3)$ and $6S_{1/2}(F=4)$ states is $(1/16)\Gamma_t$ [with Γ_t given by Eq. (4)].

In the density matrix formalism, we consider $6P_{1/2}(F', m_{F'}) \rightarrow 6S_{1/2}(F=3 \text{ or } 4, m_F)$, $6P_{3/2}(F''', m_{F'''}) \rightarrow 6S_{1/2}(F=3 \text{ or } 4, m_F)$, $8S_{1/2}(F'', m_{F''}) \rightarrow 6P_{1/2}(F', m_{F'})$, and $8S_{1/2}(F'', m_{F''}) \rightarrow 6P_{3/2}(F''', m_{F'''})$ fluorescence and absorption

of laser photons on the pump [$6S_{1/2}(F=4) \rightarrow 6P_{1/2}(F')$] and probe [$6P_{1/2}(F') \rightarrow 8S_{1/2}(F'')$] transitions. The terms $|V_{ij}|^2$, which represent absorption and stimulated emission, are proportional to the fluorescence rates Γ_{ij} according to Eq. (14). Thus, we need to determine the branching ratios for fluorescence decay rates between individual magnetic sublevels of the two hyperfine levels under consideration. These, in turn, are proportional to the square of the dipole matrix elements; for example,

$$\Gamma_{6P_{1/2}(F',m_{F'}) \rightarrow 6S_{1/2}(F,m_F)} \propto |\langle 6P_{1/2}(F',m_{F'}) | \vec{r} | 6S_{1/2}(F,m_F) \rangle|^2. \quad (29)$$

Using standard angular momentum coupling theory [35], the right-hand side of Eq. (29) can be written in terms of reduced matrix elements $\langle 6P_{1/2} | r | 6S_{1/2} \rangle$ and angular momentum coupling constants $C_{F'm_{F'},Fm_F}$ and $C_{F',F}$:

$$\begin{aligned} \Gamma_{6P_{1/2}(F',m_{F'}) \rightarrow 6S_{1/2}(F,m_F)} &\propto |C_{F'm_{F'},Fm_F}|^2 \\ &\quad \times |\langle 6P_{1/2}(F') | r | 6S_{1/2}(F) \rangle|^2 \\ &\propto |C_{F'm_{F'},Fm_F}|^2 |C_{F',F}|^2 \\ &\quad \times |\langle 6P_{1/2} | r | 6S_{1/2} \rangle|^2 \\ &= |C_{F'm_{F'},Fm_F}|^2 |C_{F',F}|^2 \Gamma_{6P_{1/2} \rightarrow 6S_{1/2}}, \end{aligned} \quad (30)$$

where the factors $|C_{F'm_{F'},Fm_F}|^2$ and $|C_{F',F}|^2$ can be determined from, for example, the tables on pp. 63 and 69 of Condon and Shortley [35], and the coefficients are normalized such that

$$\sum_{F,m_F} |C_{F'm_{F'},Fm_F}|^2 |C_{F',F}|^2 = 1.$$

For our calculations, we use the $6P_{1/2}$ and $6P_{3/2}$ radiative rates ($\Gamma_{6P_{1/2} \rightarrow 6S_{1/2}} = 2.851 \times 10^7 \text{ s}^{-1}$ and $\Gamma_{6P_{3/2} \rightarrow 6S_{1/2}} = 3.271 \times 10^7 \text{ s}^{-1}$) from the accurate lifetime measurements of Rafac *et al.* [36] and the $8S_{1/2} \rightarrow 6P_{1/2}$ and $8S_{1/2} \rightarrow 6P_{3/2}$ rates ($\Gamma_{8S_{1/2} \rightarrow 6P_{1/2}} = 1.969 \times 10^6 \text{ s}^{-1}$ and $\Gamma_{8S_{1/2} \rightarrow 6P_{3/2}} = 3.618 \times 10^6 \text{ s}^{-1}$) from calculations of gf values by Warner [37].

In general, the coherence relaxation terms are given by [32]

$$\delta_{ij} = \frac{1}{2}(\Gamma_i + \Gamma_j) + \delta_{ij}^{\text{col}}, \quad (31)$$

where Γ_i and Γ_j represent the total decay rates for levels i and j , respectively, and δ_{ij}^{col} is the dipole dephasing rate due to processes that are not associated with the transfer of population (e.g., elastic collisions). For our calculations, δ_{31}^{col} was calculated from the room temperature Cs-Ar collisional broadening rate for the Cs[$6S_{1/2}(F=4)$] hyperfine component of the D_1 line reported by Bernabeu and Alvarez [27]. For a given $6P_{1/2}(F') \rightarrow 8S_{1/2}(F'')$ transition, the δ_{53}^{col} coherence relaxation term was determined from radiative rates above (including also the $8S_{1/2} \rightarrow 7P_J$ transitions) and δ_{53}^{col} was obtained from the appropriate linear fit to the $6P_{1/2}(F') \rightarrow 8S_{1/2}(F'')$ Cs-Ar pressure broadening data reported in Sec. III of this paper. Finally, since δ_{51}^{col} was not known, we ap-

proximated its value with δ_{53}^{col} and determined the δ_{51} coherence relaxation term from the total radiative decay rate of population out of the $8S_{1/2}$ state and the collisional broadening rate for the appropriate $6P_{1/2}(F') \rightarrow 8S_{1/2}(F'')$ transition.

The quantity of interest that is measured in the experiment is the total $8S_{1/2}(F'') \rightarrow 6P_{3/2}$ fluorescence, which is detected at right angles to the laser propagation axis by a free-standing photomultiplier tube equipped with appropriate filters. The system is equally sensitive to fluorescence polarized parallel to and perpendicular to the laser propagation axis. Under these conditions, the detection system is twice as sensitive to $\Delta m_F = 0$ fluorescence transitions ($I \propto |\langle 8S_{1/2}(F'',m_{F''}) | z | 6P_{3/2}(F''',m_{F'''}) \rangle|^2$) as it is to $\Delta m_F = \pm 1$ transitions ($I \propto |\langle 8S_{1/2}(F'',m_{F''}) | x \pm iy | 6P_{3/2}(F''',m_{F'''} = m_{F''} \pm 1) \rangle|^2$). It is therefore straightforward to show that if the final hyperfine state F''' is not resolved, then the detected fluorescence signal associated with each upper state magnetic sublevel $I_{8S_{1/2}(F'',m_{F''}) \rightarrow 6P_{3/2}}$ is proportional to the population $n_{8S_{1/2}(F'',m_{F''})}$ in that $8S_{1/2}(F'',m_{F''})$ sublevel, with the same proportionality factor for each sublevel. Thus we assume that the total $8S_{1/2}(F'')$ population [$n_{8S_{1/2}(F'')} = \sum_{m_{F''}} n_{8S_{1/2}(F'',m_{F''})}$] is simply proportional to the total $8S_{1/2}(F'') \rightarrow 6P_{3/2}$ fluorescence measured for the appropriate pump-probe scheme.

For $6S_{1/2}(F=4) \rightarrow 6P_{1/2}(F'=3)$ pumping and a given collisional transfer rate $k_{6P_{1/2}(F'=3 \rightarrow F'=4)}^{\text{hfs}} n_{\text{Ar}}$ (noting that the very small back transfer can be taken into account approximately by using the value $k_{6P_{1/2}(F'=4 \rightarrow F'=3)}^{\text{hfs}} n_{\text{Ar}} = 0.78 k_{6P_{1/2}(F'=3 \rightarrow F'=4)}^{\text{hfs}} n_{\text{Ar}}$ from the principle of detailed balance as discussed above), we solve the density matrix equations to determine the ratio $n_{8S_{1/2}(F''=3)}^{\text{collisional}} / (n_{8S_{1/2}(F''=3)}^{\text{direct}} + n_{8S_{1/2}(F''=4)}^{\text{direct}})$. In these expressions, the superscript ‘‘direct’’ (‘‘collisional’’) indicates that the probe laser is coupled to the directly excited (collisionally populated) $6P_{1/2}(F')$ level [i.e., $n_{8S_{1/2}(F''=3)}^{\text{collisional}}$ for $6P_{1/2}(F'=3)$ pumping is the total population in the $8S_{1/2}(F''=3)$ level when the pump-probe scheme is $6S_{1/2}(F=4) \rightarrow 6P_{1/2}(F'=3) \xrightarrow{\text{collision}} 6P_{1/2}(F'=4) \rightarrow 8S_{1/2}(F''=3)$ and $n_{8S_{1/2}(F''=3)}^{\text{direct}}$ is the population in the $8S_{1/2}(F''=3)$ level when the pump-probe scheme is $6S_{1/2}(F=4) \rightarrow 6P_{1/2}(F'=3) \rightarrow 8S_{1/2}(F''=3)$]. Absorption of probe laser photons is detected by monitoring $8S_{1/2}(F'') \rightarrow 6P_{3/2}$ fluorescence intensities, and the integrated intensity of each transition is proportional to the population in the $8S_{1/2}(F'')$ state. Hence the calculated population ratios are compared to $I_{8S_{1/2}(F''=3) \rightarrow 6P_{3/2}}^{\text{collisional}} / (I_{8S_{1/2}(F''=3) \rightarrow 6P_{3/2}}^{\text{direct}} + I_{8S_{1/2}(F''=4) \rightarrow 6P_{3/2}}^{\text{direct}})$ values, which are determined from the integrated areas under the excitation lines (see Fig. 8). The value of $k_{6P_{1/2}(F'=3 \rightarrow F'=4)}^{\text{hfs}} n_{\text{Ar}}$ is adjusted until the experimental and calculated population ratios agree. The method converges quickly since the population ratio is approximately proportional to $k_{6P_{1/2}(F'=3 \rightarrow F'=4)}^{\text{hfs}} n_{\text{Ar}}$. For $6S_{1/2}(F=4) \rightarrow 6P_{1/2}(F'=4)$ pumping, the same procedure is followed with $k_{6P_{1/2}(F'=4 \rightarrow F'=3)}^{\text{hfs}} n_{\text{Ar}}$ being adjusted and, in this case, the ratios of

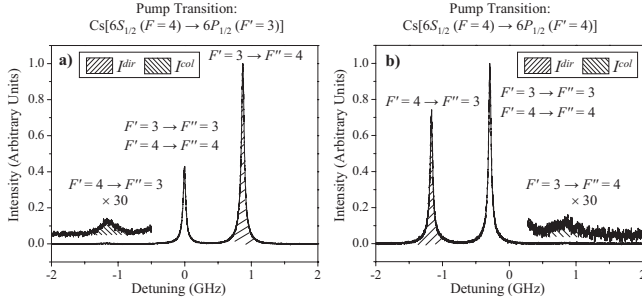


FIG. 8. Excitation spectra associated with the two possible Cs[$6S_{1/2}(F=4) \rightarrow 6P_{1/2}(F')$] pump laser transitions: (a) $F'=3$; (b) $F'=4$. In each case the area under the “direct” peak [$F=4 \rightarrow F'=3 \rightarrow F''=4$ or $F=4 \rightarrow F'=4 \rightarrow F''=3$] is represented by positively sloped hash marks while the area under the “collisional” peak ($F=4 \rightarrow F'=3 \rightarrow F''=3$ or $F=4 \rightarrow F'=4 \rightarrow F''=3$ or $F=4 \rightarrow F'=4 \rightarrow F''=4$) is represented by negatively sloped hash marks. The ratios of interest are $I_{8S_{1/2}(F''=3) \rightarrow 6P_{3/2}}^{\text{collisional}} / (I_{8S_{1/2}(F''=3) \rightarrow 6P_{3/2}}^{\text{direct}} + I_{8S_{1/2}(F''=4) \rightarrow 6P_{3/2}}^{\text{direct}})$ in (a) and $I_{8S_{1/2}(F''=4) \rightarrow 6P_{3/2}}^{\text{collisional}} / (I_{8S_{1/2}(F''=3) \rightarrow 6P_{3/2}}^{\text{direct}} + I_{8S_{1/2}(F''=4) \rightarrow 6P_{3/2}}^{\text{direct}})$ in (b). The middle peak is a superposition of a strong direct peak with a weak collisional peak and is not shaded in the figure. However, in each case, the collisional contribution to this peak is very small, and the area associated with the directly pumped excitation line shape (i.e., the Lorentzian portion of the middle peak) is used in the determination of the ratio of interest.

interest are $I_{8S_{1/2}(F''=4) \rightarrow 6P_{3/2}}^{\text{collisional}} / (n_{8S_{1/2}(F''=3)}^{\text{direct}} + n_{8S_{1/2}(F''=4)}^{\text{direct}})$ and $I_{8S_{1/2}(F''=4) \rightarrow 6P_{3/2}}^{\text{collisional}} / (I_{8S_{1/2}(F''=3) \rightarrow 6P_{3/2}}^{\text{direct}} + I_{8S_{1/2}(F''=4) \rightarrow 6P_{3/2}}^{\text{direct}})$.

The hyperfine state-changing collision rates [$R_{34} = k_{6P_{1/2}(F'=3 \rightarrow F'=4)}^{\text{hfs}} n_{\text{Ar}}$ and $R_{43} = k_{6P_{1/2}(F'=4 \rightarrow F'=3)}^{\text{hfs}} n_{\text{Ar}}$] were determined in this manner at each argon density and then plotted as a function of argon density (see Fig. 9). Since the measured intensity ratios, $I_{8S_{1/2}(F''=3) \rightarrow 6P_{3/2}}^{\text{collisional}} / (I_{8S_{1/2}(F''=3) \rightarrow 6P_{3/2}}^{\text{direct}} + I_{8S_{1/2}(F''=4) \rightarrow 6P_{3/2}}^{\text{direct}})$ and $I_{8S_{1/2}(F''=4) \rightarrow 6P_{3/2}}^{\text{collisional}} / (I_{8S_{1/2}(F''=3) \rightarrow 6P_{3/2}}^{\text{direct}} + I_{8S_{1/2}(F''=4) \rightarrow 6P_{3/2}}^{\text{direct}})$, are approximately proportional to the collision rates, $k_{6P_{1/2}(F'=3 \rightarrow F'=4)}^{\text{hfs}} n_{\text{Ar}}$ and $k_{6P_{1/2}(F'=4 \rightarrow F'=3)}^{\text{hfs}} n_{\text{Ar}}$, the uncertainties in the fitted collisional rates arise from uncertainties in the intensity ratios and in the argon pressure, with the latter being more significant at low pressures and the former dominating at high pressures. From weighted linear least squares fits, the hyperfine state-changing collision rate coefficients were determined:

$$k_{6P_{1/2}(F'=3 \rightarrow F'=4)}^{\text{hfs}} = (2.39 \pm 0.15) \times 10^{-11} \text{ cm}^3 \text{ sec}^{-1} \quad (32)$$

and

$$k_{6P_{1/2}(F'=4 \rightarrow F'=3)}^{\text{hfs}} = (1.77 \pm 0.17) \times 10^{-11} \text{ cm}^3 \text{ sec}^{-1}. \quad (33)$$

Since $E_{F'=4} - E_{F'=3} \ll k_B T$, the principle of detailed balance states that the ratio of the hyperfine state-changing collision

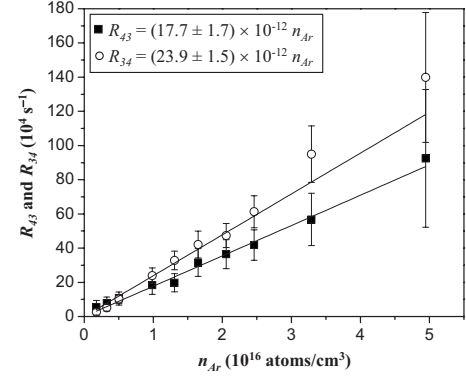


FIG. 9. Plot of the hyperfine state-changing collision rates [$R_{34} = k_{6P_{1/2}(F'=3 \rightarrow F'=4)}^{\text{hfs}} n_{\text{Ar}}$ and $R_{43} = k_{6P_{1/2}(F'=4 \rightarrow F'=3)}^{\text{hfs}} n_{\text{Ar}}$] as functions of argon density obtained from a model in which it is assumed that the final state $m_{F'}$ level is independent of the initial state $m_{F'}$ value, and hence, all final state $m_{F'}$ values are equally probable. From the linear fits to the results, the hyperfine state-changing collision rate coefficients, $k_{6P_{1/2}(F'=3 \rightarrow F'=4)}^{\text{hfs}}$ and $k_{6P_{1/2}(F'=4 \rightarrow F'=3)}^{\text{hfs}}$, were determined. Error bars represent the uncertainty in the ratio of the collisional to direct peak areas and uncertainty in the argon pressure, with the latter being more significant at low pressures and the former being dominant at high pressures.

rate coefficients $k_{6P_{1/2}(F'=4 \rightarrow F'=3)}^{\text{hfs}} / k_{6P_{1/2}(F'=3 \rightarrow F'=4)}^{\text{hfs}}$ should equal 0.78. Experimentally, from Eqs. (32) and (33) we obtain a ratio of 0.74 ± 0.11 . We believe that these results indicate that the $m_{F'}$ value is essentially scrambled during the hyperfine state-changing collision as we assume. This is not surprising given the small magnitudes of the rate coefficients, which again indicate that excitation transfer from one hyperfine state to another requires strong collisions at small impact parameter.

Although the assumption that the $m_{F'}$ levels are completely scrambled in the hyperfine state-changing collisions may not be strictly valid, especially given that the measured $6P_{1/2}$ state depolarization rate is small [26], we have also carried out an analysis of our data using a model based on the opposite limiting case—namely that the $m_{F'}$ value is conserved during the Cs[$6P_{1/2}(F'=3)$] + Ar \leftrightarrow Cs[$6P_{1/2}(F'=4)$] + Ar process. Those results agree with the reported results to within 25%. Therefore, we believe that the magnitudes of the hyperfine state-changing collision rate coefficients are not strongly dependent on the validity of this assumption concerning the mixing of the $m_{F'}$ levels.

VI. CONCLUSIONS

We have carried out a two-step excitation experiment to study Cs-Ar collisions that transfer population between the two hyperfine levels of the Cs($6P_{1/2}$) state. Via a density matrix analysis, we have determined the Cs($6P_{1/2}$)-Ar hyperfine state-changing collision rate coefficients assuming that $m_{F'}$ levels are populated statistically by the collisional transfer process. A comparison of the ratio of the collisional rate coefficients obtained experimentally (0.74) to that expected

from the principle of detailed balance (0.78) indicates that this assumption is reasonable, but it should be noted that the results are not particularly sensitive to this assumption.

We can define velocity averaged hyperfine state-changing collision cross sections by the expression $\sigma_{6P_{1/2}(F_1 \rightarrow F_2)}^{\text{hfs}} \equiv k_{6P_{1/2}(F_1 \rightarrow F_2)}^{\text{hfs}} / \bar{v}$ where \bar{v} is the average collision speed. Using $\bar{v} \sim 4.5 \times 10^4$ cm/s at our cell temperature, we obtain

$$\sigma_{6P_{1/2}(F'=3 \rightarrow F'=4)}^{\text{hfs}} = (5.3 \pm 0.3) \times 10^{-16} \text{ cm}^2 \quad (34)$$

and

$$\sigma_{6P_{1/2}(F'=4 \rightarrow F'=3)}^{\text{hfs}} = (3.9 \pm 0.4) \times 10^{-16} \text{ cm}^2. \quad (35)$$

We are not aware of any theoretical calculations of these cross sections, but we note that the measured values are factors of only 2–3 times greater than the small cross sections for depolarization of Cs($6P_{1/2}$) atoms in collisions with argon measured by Gallagher [26]. The mechanisms for depolarization and hyperfine state-changing collisions are likely to be related since both processes require $M_J=1/2 \leftrightarrow M_J=-1/2$ for $J=1/2$ (assuming that $\Delta M_J=0$). Gallagher showed that $P_{1/2}$ state depolarization cross sections should decrease rapidly as the fine-structure interval ΔE_J increases beyond \hbar/τ_c , where τ_c is the collision duration. In the limit $\Delta E_J \gg \hbar/\tau_c$, he showed that $M_J \leftrightarrow -M_J$ is forbidden for a model that assumes an odd total number of electrons (active atom plus perturber), a time-reversal invariant Hamiltonian, and neglect of nonadiabatic terms [26,38]. In the present case, $\hbar/\tau_c \sim 8$ cm $^{-1}$ is indeed small compared to the $6P$ level fine structure splitting ($\Delta E_J \sim 554$ cm $^{-1}$), so this model should be valid. An accurate calculation of either the Cs($6P_{1/2}$) depolarization or hyperfine state-changing collision cross section would therefore depend only on smaller nonadiabatic interaction terms and would be sensitive to details of the interatomic Cs-Ar potentials [39,40], specifically on the repulsive short range region. However, the cross section is expected to depend sharply on the spin-orbit separation [without making assumptions about trajectory or the interaction except that it is purely electrostatic, Gallagher's Eq. (7) leads to the prediction that the depolarization cross section should scale as ΔE_J^{-2} —see also Fig. 3 of Ref. [38]]. The hyperfine state-changing collision cross section, as well as the depolarization cross section, are expected to be signifi-

cantly larger in the Cs($6P_{3/2}$) state where $M_J \leftrightarrow -M_J$ is not required.

Besides determining the collisional rate coefficients, our data also provide information concerning the velocity along the laser propagation direction for Cs[$6P_{1/2}(F')$] atoms, which initially all have $v_z=0$, that have undergone a single Cs[$6P_{1/2}(F'=3)$]+Ar \leftrightarrow Cs[$6P_{1/2}(F'=4)$]+Ar hyperfine state-changing collision. Our results, which indicate that significant velocity changes do occur in single hyperfine state-changing collisions, are also consistent with the fact that Cs[$6P_{1/2}(F'=3)$]+Ar \leftrightarrow Cs[$6P_{1/2}(F'=4)$]+Ar hyperfine mixing requires $M_J=1/2 \leftrightarrow M_J=-1/2$ depolarizing collisions. In contrast to previous Na($3P_{3/2}$) \rightarrow Na($3P_{1/2}$) fine structure state-changing collisions where relatively small velocity changes were observed [10], our results support an idea introduced by Gallagher [26] and Gibbs *et al.* [38] that $J=1/2$ state depolarization only occurs through strong collisions at small impact parameter. Consequently, collisions that transfer population between hyperfine levels of the Cs($6P_{1/2}$) state are associated with larger velocity changes than those previously observed for Na fine structure state-changing collisions.

We have also analyzed the experimental line shapes resulting from direct pump-probe excitation to yield the $6P_{1/2}(F') \rightarrow 8S_{1/2}(F'')$ argon pressure broadening rates and shifts. The uncertainties in our reported values are smaller than the differences between the pressure broadening rate coefficients for the four hyperfine components, implying that these differences are real. Therefore, our reported values should provide stringent checks for the quality of current *ab initio* and model potential calculations for long range Cs[$6P_{1/2}(F')$]-Ar and Cs[$8S_{1/2}(F'')$]-Ar interatomic potentials.

ACKNOWLEDGMENTS

The authors would like to thank Goran Pichler, Kurt Gibble, and Alan Streater for useful discussions and Charles Sukenik for providing a list of the available alkali-noble gas interaction potentials. This work was supported by the National Science Foundation (Grant No. PHY-0244767). L.M. was partially supported by a Drew University Faculty Release Time Grant and T.D. was supported by the NSF REU site grant in the Department of Physics at Lehigh University.

-
- [1] H. M. Pickett, J. Chem. Phys. **73**, 6090 (1980).
 [2] M. Bornstein and W. E. Lamb, Jr., Phys. Rev. A **5**, 1311 (1972).
 [3] J. Apt and D. E. Pritchard, Phys. Rev. Lett. **37**, 91 (1976).
 [4] P. F. Liao, J. E. Bjorkholm, and P. R. Berman, Phys. Rev. A **21**, 1927 (1980).
 [5] W. A. Hamel, J. E. M. Haverkort, H. G. C. Werij, and J. P. Woerdman, J. Phys. B **19**, 4127 (1986).
 [6] G. Nienhuis and S. Kryszewski, Phys. Rev. A **36**, 1305 (1987).
 [7] J. E. M. Haverkort, J. P. Woerdman, and P. R. Berman, Phys.

- Rev. A **36**, 5251 (1987).
 [8] H. G. C. Werij and J. P. Woerdman, Phys. Rep. **169**, 145 (1988).
 [9] M. J. O'Callaghan and J. Cooper, Phys. Rev. A **39**, 6206 (1989).
 [10] M. J. O'Callaghan and A. Gallagher, Phys. Rev. A **39**, 6190 (1989).
 [11] K. E. Gibble and J. Cooper, Phys. Rev. A **44**, R5335 (1991).
 [12] K. E. Gibble and J. Cooper, Phys. Rev. Lett. **67**, 1936 (1991).
 [13] K. E. Gibble and A. Gallagher, Phys. Rev. A **43**, 1366 (1991).

- [14] G. Shimkaveg, W. W. Quivers, Jr., R. R. Dasari, and M. S. Feld, *Phys. Rev. A* **48**, 1409 (1993).
- [15] R. K. Namiotka, E. Ehrlacher, J. Sagle, M. Brewer, D. J. Namiotka, A. P. Hickman, A. D. Streater, and J. Huennekens, *Phys. Rev. A* **54**, 449 (1996).
- [16] R. Ciuryło, D. Lisak, and J. Szudy, *Phys. Rev. A* **66**, 032701 (2002).
- [17] Y. Ohta, M. Hasuo, and T. Fujimoto, *Opt. Commun.* **210**, 245 (2002).
- [18] F. Kh. Gel'mukhanov and A. I. Parkhomenko, *Zh. Eksp. Teor. Fiz.* **108**, 1589 (1995).
- [19] W. D. Phillips, C. L. Glaser, and D. Kleppner, *Phys. Rev. Lett.* **38**, 1018 (1977).
- [20] C. G. Aminoff, J. Javanainen, and M. Kaivola, *Phys. Rev. A* **28**, 722 (1983).
- [21] T. W. Mossberg, R. Kachru, and S. R. Hartmann, *Phys. Rev. Lett.* **44**, 73 (1980).
- [22] J. C. Keller and J. L. Le Gouët, *Phys. Rev. A* **32**, 1624 (1985).
- [23] T. C. Morgus, S. J. Rohn, and A. D. Streater, *Phys. Rev. A* **57**, 4983 (1998).
- [24] J. Apt and D. E. Pritchard, *J. Phys. B* **12**, 83 (1979).
- [25] D. Lemoine, J. M. Robbe, and B. Pouilly, *J. Phys. B* **21**, 1007 (1988).
- [26] A. Gallagher, *Phys. Rev.* **157**, 68 (1967).
- [27] E. Bernabeu and J. M. Alvarez, *Phys. Rev. A* **22**, 2690 (1980).
- [28] E. Bernabeu, F. G. Peralta, and J. M. Alvarez, *J. Opt. Soc. Am.* **67**, 24 (1977).
- [29] A. N. Nesmeyanov, *Vapor Pressure of the Elements* (Academic Press, New York, 1963).
- [30] J. Sagle, R. K. Namiotka, and J. Huennekens, *J. Phys. B* **29**, 2629 (1996).
- [31] F. C. Spano, *J. Chem. Phys.* **114**, 276 (2001).
- [32] Robert W. Boyd, *Nonlinear Optics* (Academic Press, San Diego, 1992).
- [33] J. Sagle, Ph.D. thesis, Lehigh University, 1996.
- [34] L. Krause, in *The Excited State in Chemical Physics*, edited by J. W. McGowan (Wiley, New York, 1975), p. 267.
- [35] E. U. Condon and G. H. Shortley, *The Theory of Atomic Spectra* (Cambridge University Press, Cambridge, UK, 1991).
- [36] R. J. Rafac, C. E. Tanner, A. E. Livingston, and H. G. Berry, *Phys. Rev. A* **60**, 3648 (1999).
- [37] B. Warner, *Mon. Not. R. Astron. Soc.* **139**, 115 (1968).
- [38] H. M. Gibbs, G. G. Churchill, T. R. Marshall, J. F. Papp, and F. A. Franz, *Phys. Rev. Lett.* **25**, 263 (1970).
- [39] J. Pascale and J. Vandeplanque, *J. Chem. Phys.* **60**, 2278 (1974).
- [40] E. Czuchaj and J. Sienkiewicz, *Z. Naturforsch. A* **34**, 694 (1979).